

# Daytime sky brightness characterization for persistent GEO SSA

Grant M. Thomas

*Air Force Institute of Technology, Wright-Patterson AFB, Ohio*

Richard G. Cobb

*Air Force Institute of Technology, Wright-Patterson AFB, Ohio*

## ABSTRACT

Space Situational Awareness (SSA) is fundamental to operating in space. SSA for collision avoidance ensures safety of flight for both government and commercial spacecraft through persistent monitoring. A worldwide network of optical and radar sensors gather satellite ephemeris data from the nighttime sky. Current practice for daytime satellite tracking is limited exclusively to radar as the brightening daytime sky prevents the use of visible-band optical sensors. Radar coverage is not pervasive and results in significant daytime coverage gaps in SSA. To mitigate these gaps, optical telescopes equipped with sensors in the near-infrared band (0.75-0.9 $\mu$ m) may be used. The diminished intensity of the background sky radiance in the near-infrared band may allow for daylight tracking further into the twilight hours. To determine the performance of a near-infrared sensor for daylight custody, the sky background radiance must first be characterized spectrally as a function of wavelength. Using a physics-based atmospheric model with access to near-real time weather, we developed a generalized model for the apparent sky brightness of the Geostationary satellite belt. The model results are then compared to measured data collected from Dayton, OH through various look and Sun angles for model validation and spectral sky radiance quantification in the visible and near-infrared bands.

## 1 INTRODUCTION

Spectral sky radiance or spectral sky brightness is a measure of the radiant intensity at each wavelength of the atmosphere. In this paper, sky radiance (or brightness) refers to the line-by-line radiometric intensity and not the integrated or total radiometric intensity as is sometimes referenced by astronomers. Understanding daytime sky brightness radiance and transmission as a function of wavelength and location is critical for persistent optical space situational awareness (SSA) sensors. 24/7 custody of satellites is desirable and legacy SSA systems rely on an integrated network of both optical and radar sources to monitor orbiting spacecraft. Daylight custody is almost exclusively conducted with radar and thus extending the optical detection window of a satellite any amount beyond the daytime terminator condition by smaller and more agile sensors is of interest. Geosynchronous satellites, due to their range, are very difficult to track with all but the most sophisticated radar. The daytime sky is typically too bright to image a satellite in the visible band, however decreased spectral sky radiance in the near-infrared (NIR) band indicates that imaging at these wavelengths may be possible. The widespread availability of near-infrared sensors and the diminished spectral sky radiance background noise in this band as compared to the visible for a given Sun angle, make it of particular interest. As sensor development improves and the demand for pervasive SSA increases, more research is necessary to determine the feasibility of a daytime optical system in the NIR.

The brightening daytime sky acts as a rising noise-floor which quickly overwhelms the satellite signal. This is especially true in the visible wavelengths where the near blackbody emission of the Sun's radiant energy peaks due to its temperature. However, in longer wavelengths such as the NIR, the sky background radiance is not as bright as the visible for a given Sun angle. Increased SNR ratios in the NIR may extend the capability of a sensor location to image into the twilight hours. Daytime sky brightness measurements of the GEO-belt in the NIR and short-wave infrared (SWIR) do exist. However, most research focuses

on premiere imaging locations such as Haleakala, HI [1] which have exceptionally clear skies. Most other imaging locations, while still of interest, suffer from greater aerosol counts and dynamic weather conditions. The net result is increased scattering effects in both the visible and near-infrared (Vis-NIR) bands resulting in higher sky radiance background noise and thereby decreasing signal detectability [2].

At present, most optical system designers rely heavily on atmospheric models such as the Laser Environmental Effects Definition and Reference (LEEDR) or MODerate resolution atmospheric TRANsmission (MODTRAN) code to simulate real-world conditions with enough fidelity to characterize system performance [3, 4]. This is especially true for optical sensor sites that have relatively low-visibility due to aerosols or high-humidity. The daytime Vis-NIR band spectral sky radiance measurements conducted herein help to refine and validate first-principles atmospheric models. The associated models can then be extended to a wider variety of realistic atmospheric conditions at a greater diversity of imaging locations.

## 1.1 Background

The spectral radiance of the daytime sky is dependent on the time of day, season, atmospheric constituents and conditions. These conditions are in a state of constant fluctuation and may cause the spectral radiance of the sky to vary greatly from day to day. To model or predict sky brightness, first-principle atmospheric models propagate the spectral radiance of the Sun to a sensor through representative atmospheric layers. Accurate results are possible by capturing the dominant radiometric transfer physics and atmospheric attenuation of each layer.

The direct solar radiation coming to Earth from the Sun is attenuated by the atmospheric absorption and scattering [5]. Sunlight interacts with atmospheric particles and molecules scattering through single and multiple processes resulting in spectral radiance [5]. This detectable sky brightness can be separated into diffuse and direct components which are primarily a function of two mechanisms: scattered radiation from the Sun and emission by atmospheric constituents [5, 6]. For visible through short-wave infrared wavelengths, scattering is critical during the daytime. At wavelengths longer than  $4\mu\text{m}$  the sky radiance detected is almost exclusively due to thermal atmospheric emission [6]. The emitted radiation from atmospheric constituents is present both night and day. This research will focus on Vis-NIR wavelengths from  $0.4\mu\text{m}$  to  $0.9\mu\text{m}$  and consider aerosol scattering as the primary sky brightening mechanism.

When sunlight propagates through a scattering medium (such as the atmosphere) it can be absorbed as well as scattered away from the direction of propagation [7]. Both absorption and scattering are loss mechanisms. For a homogeneous layer of the atmosphere, the combined effect of the scattering and absorption is characterized by the extinction coefficient  $\beta_e$  where,  $\beta_a$  is the absorption coefficient and  $\beta_s$  is the scattering coefficient.

$$\beta_e = \beta_a + \beta_s \quad (1)$$

The absorption coefficient  $\beta_a$  is defined by the complex index of refraction ( $\kappa$ ) for the medium at each wavelength ( $\lambda$ ), thus:

$$\beta_s = \frac{4\pi\kappa}{\lambda} \quad (2)$$

Mie scattering expressions can be greatly simplified under the assumption that the size of the spherical scatterer is significantly smaller than the wavelength of incoming radiation as is the case for visible wavelengths and longer [7]. This is known as the Rayleigh scattering regime and is governed by the following expression for the scattering coefficient ( $\beta_s$ )

$$\beta_s = \frac{64M\pi^5 a^6}{3\lambda^4} \left| \frac{n^2 - 1}{n^2 + 2} \right|^2 \quad (3)$$

where,  $a$  is the radius of the spherical scatterer,  $n$  is the index of refraction in the medium, and  $M$  are the

scatterers per volume. Using Beer’s Law we can describe the irradiance transmission spectrum  $T$  for a given material thickness  $z$ .

$$T(\lambda) = \exp(-\beta_e z) \quad (4)$$

Both LEEDR and MODTRAN model the sky brightness by propagating the irradiance of a source (usually the near-blackbody radiation of the Sun) through multiple layers of distinct homogeneous atmosphere. By sequencing subsequent layers where the exiting irradiance of the previous layer becomes the entering irradiance of the next, the total effective irradiance is readily calculated. The effective irradiance of each layer after a propagation distance  $z$  given by

$$E(\lambda, z) = E(\lambda, 0) \exp(-\beta_e z) \quad (5)$$

For a Lambertian source, the spectral radiance  $L(\lambda)$  can then be calculated by

$$L(\lambda) = \frac{E(\lambda)}{\pi} \quad (6)$$

If an absolute radiance calibration of a spectrometer is performed, spectral radiance ( $L$ ) is the quantity directly measured by the sensor.

## 2 APPROACH

Modeling sky radiance for a particular ground site requires a comprehensive understanding of both the radiative transfer and the dynamic atmospheric conditions for a given time. For simplicity, we choose to model and measure the spectral radiance for a single region in the sky on the clearest weather day available. For our purposes, the GEO-belt sky location was located at a local azimuth of 180°S and an elevation of 44° from Dayton, OH. The “GEO-belt” is understood to be shorthand for the orbital ring of satellites at approximately 0° inclination and zero eccentricity that have the same orbital period as the Earth’s rotational period. An elevation of 44° is the “highest” position of the GEO-belt in the local sky. While this position is representative of the GEO-belt radiant conditions, no known satellites were in the field of during the measurement. As the highest GEO-belt location in the sky, this location provides a moderate testing environment wherein the sky spectral radiance will increase and decrease as a function of Sun angle as depicted in Figure 1.

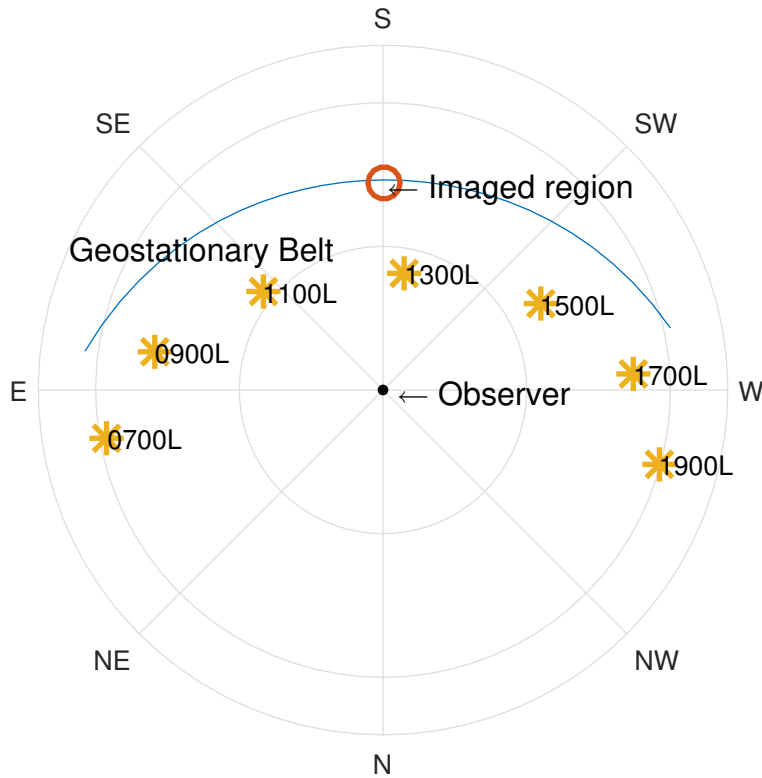


Figure 1: Top-down view of imaging geometry. The yellow asterisks correlate to Sun positions for various local times.

All tests were conducted on August 26th, 2017 wherein Dayton enjoyed exceptionally clear skies and relatively high visibility. Once the measurements were taken, a LEEDR model was generated using historical weather data, 500 distinct atmospheric layers and a representative slant path for the Sun's radiance through the atmosphere based on celestial geometry. This model was also generated for August 26th, 2017 using Global Forecast System (GFS) weather inputs.

## 2.1 Experimental setup

Sky brightness measurements were taken using an Ocean Optics USB4000 VNIR spectrometer mounted on a Meade LX200 16" telescope as in Figure 2.



Figure 2: Meade 16" reflector telescope with spectrometer pointed at zenith GEO-belt location. Note the cloudless sky which facilitated the measurement.

With this arrangement, the field of view was sufficiently narrow to ensure our measurement captured only the background spectral radiance without any contribution from orbiting satellites. The LX200-ACF Meade Schmidt-Cassegrain reflector telescope had a 406.4mm (16") aperture and a 4064mm focal length for a f/10 focal ratio. For detection by the spectrometer through the optical system, incident spectral radiation must pass through the corrector plate and reflect off the primary and secondary mirrors. The telescope mirrors are coated with Meade's "Ultra-High Transmission Coatings" which provide spectral reflectance as given in Figure 3 for the visible and near-infrared bands.

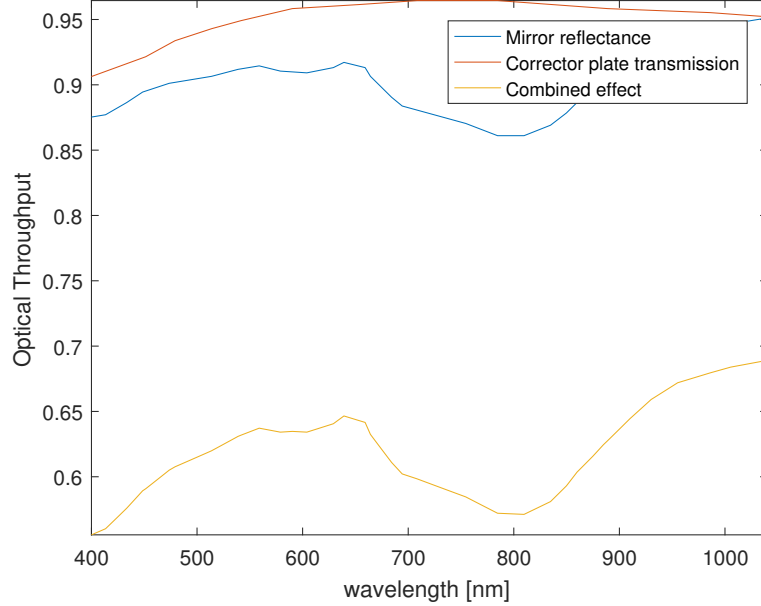


Figure 3: Estimated optical loss through Meade LX200-ACF telescope corrector plate and mirrors with Ultra-High Transmission Coatings. The spectral mirror reflectance and corrector plate transmission values are derived from measurements taken by the University of Arizona on a Meade LX-10 telescope with similar UHTC coatings [8]. Ocean Optics 1m long fiber optic cable connected the spectrometer to the telescope and was assumed to have a uniform 20% loss at all wavelengths to account for entrance and transmission losses. The combined effect of all losses through the optical system including the fiber optic cable is calculated by wavelength in Equation 7.

The spectral reflectance and transmission values are estimated from transmission and reflectance measurements taken by Schwab et al. from the University of Arizona on a Meade LX-10 telescope with similar UHTC coatings [8]. From these estimated loss values, the total spectral radiance is calculated in Equation 7:

$$Total_{loss}(\lambda) = Reflectance_1(\lambda) * Reflectance_2(\lambda) * Corrector_{loss}(\lambda) * Fiber_{loss}(\lambda) \quad (7)$$

The losses associated with mirror reflection and corrector plate transmission reduce the radiant throughput of the system, but do not inhibit spectral measurements at wavelengths less than  $2.4\mu\text{m}$  [8]. The estimated spectral loss will be applied to the model data to mimic the radiant loss experienced by the radiant energy through the telescope. The optical loss through the telescope is only an estimate and could later be refined for more accurate correlation.

The Ocean Optics USB4000 spectrometer is responsive between  $.35\text{-}0.9\mu\text{m}$  using a 3648-element CCD array from Toshiba, product number TCD1304AP [9]. The TCD1304AP sensor is a high sensitivity and low dark current linear imaging sensor with an individual pixel size of  $1600\mu\text{m}^2$  [10] and a spectral resolution of 0.1nm (full-width half-max). The spectrometer was connected via optical fiber to the primary optic of the Meade LX200 telescope as shown in Figure 4. The telescope was pointed at a local GEO-belt sky location of  $180^\circ$  azimuth and  $44^\circ$  elevation from Dayton, OH for the duration of the testing.

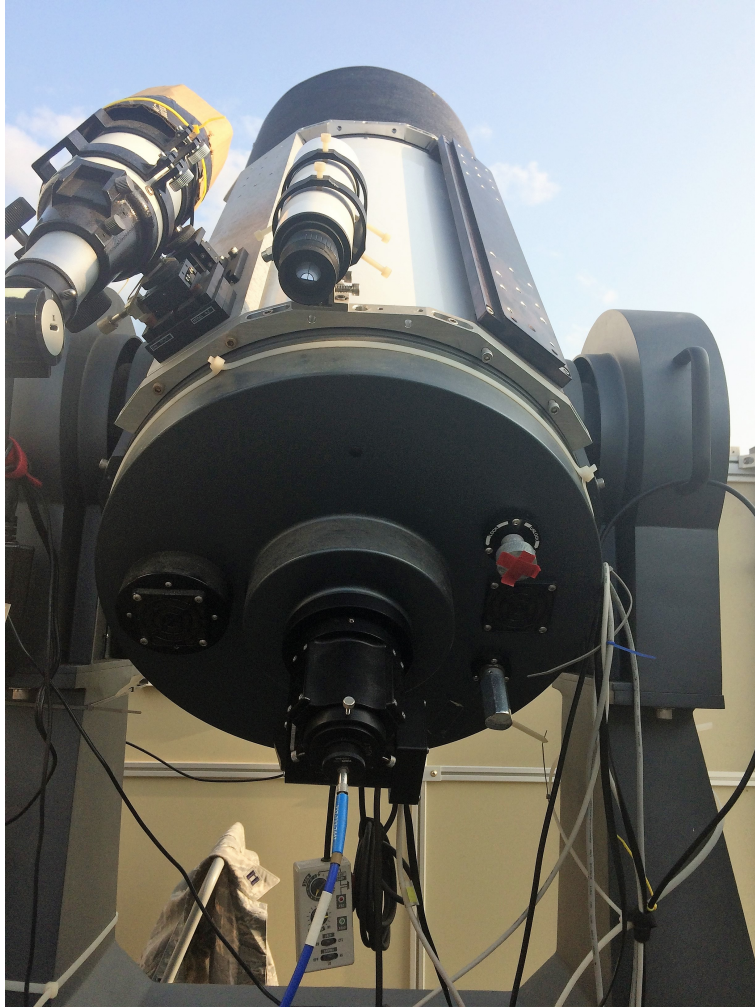


Figure 4: Ocean Optics USB4000 spectrometer connected to primary optic of AFIT telescope via optical fiber.

### 2.1.1 Spectrometer Calibration

One difficulty in correlating measured data with modeled data from LEEDR is that model data is given in terms of absolute irradiance which is a measure of the flux of radiant energy per unit area. It is therefore necessary to correlate the measured relative intensity to a known spectral source to determine the relationship between spectrally detected photons and the corresponding radiant energy.

For accurate measurements, the spectrometer should be calibrated both radiometrically (in terms of detected intensity) as well as spectrally (in terms of wavelength). The USB4000 spectrometer was spectrally calibrated by connecting directly to Ocean Optics HG-1 Mercury Argon calibration light source. The HG-1 lamp produces multiple spectral peaks at various predetermined wavelengths across the visible and NIR bands as shown in Figure 5.

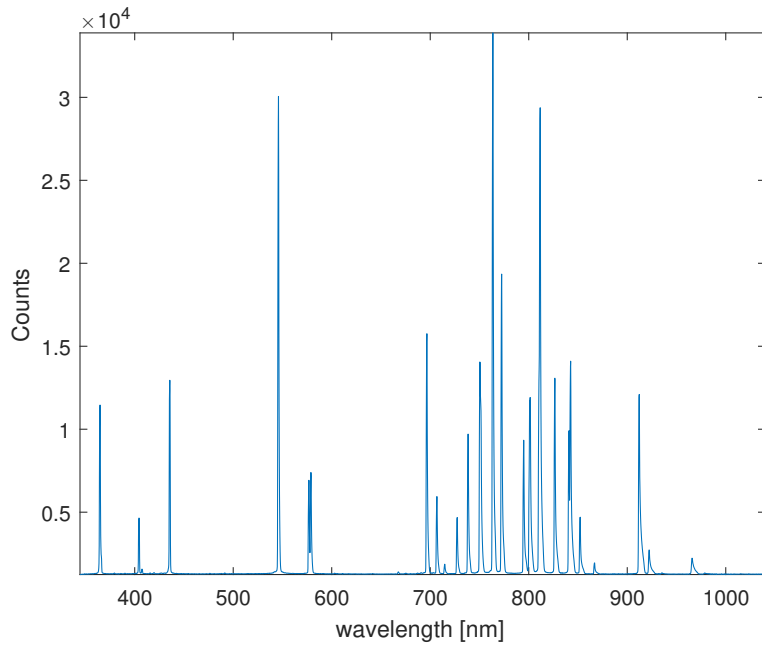


Figure 5: Ocean Optics HG-1 Mercury Argon calibration source as detected by the USB4000 spectrometer for spectral calibration. This source was used to spectrally calibrate the Ocean Optics USB4000 spectrometer.

The measured spectral peaks were compared to the known spectra for a maximum, minimum and mean  $\Delta\lambda$  of 0.48nm, 0.04nm and 0.130nm respectively. For the purposes of this measurement, the spectral calibration of the USB4000 was assumed to be sufficiently accurate and no additional spectral calibration was applied to the measured sky radiance data. Figure 6 shows the spectral correlation between the calibration peaks.

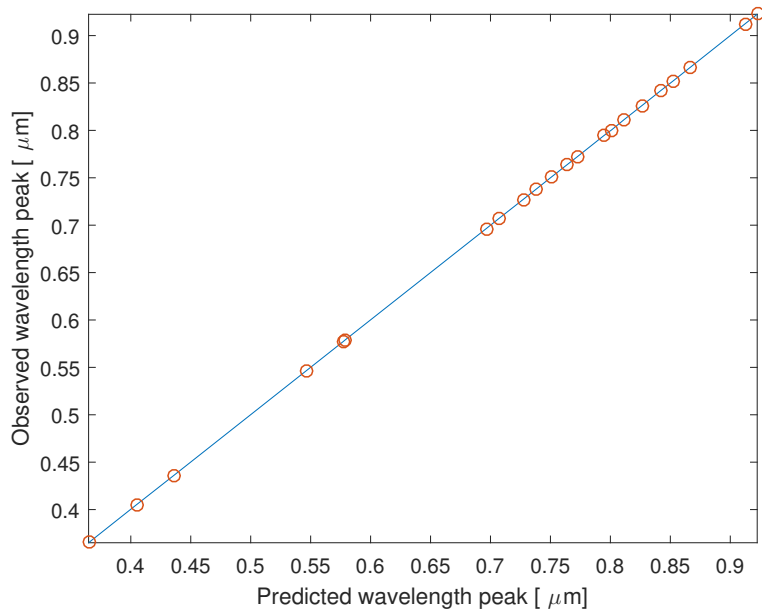


Figure 6: Observed and predicted wavelength peak locations from spectral calibration measurement Figure 5. The solid blue line indicates the perfect agreement between observed and theory, while the red circles indicate the HgAr peaks as measured from the spectrometer.

The radiometric calibration is calculated through a series of dark and reference spectra taken to correlate

the spectral gain and offset of each pixel. In our case however, there was considerable difficulty in obtaining a Blackbody reference spectra that will flood the entire field of view of the telescope main optic. As an alternative, we choose to disconnect the spectrometer from the telescope and calibrate the spectrometer individually by using an Oriel Instruments Tungsten filament calibration lamp. By placing the fiber optic cable of the spectrometer 0.5m in front of the Quartz Tungsten Halogen lamp as prescribed by Oriel, National Institute of Standards and Technology (NIST) certified spectral irradiance values are detectable at the irradiance plane as shown in Figure 7.

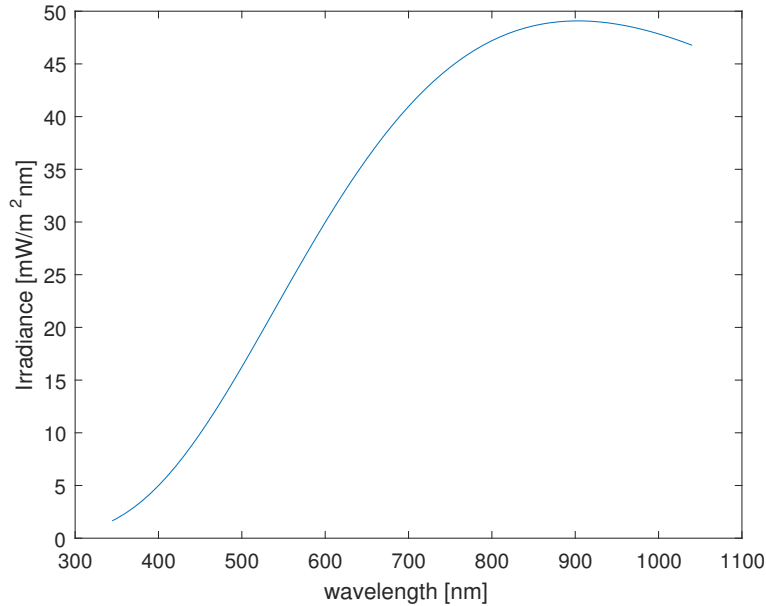


Figure 7: Oriel Instruments Tungsten Filament Lamp Model 5-123 spectral irradiance at 0.5m from the source. This source was used to radiometrically calibrate the Ocean Optics USB4000 spectrometer.

This calibration scheme provides a basic framework to compare measured radiant intensity with the modeled spectral radiance from LEEDR.

### 2.1.2 LEEDR Model

LEEDR is a validated atmospheric characterization and radiative transfer model generator[3]. Vertical profiles of temperature, pressure, water vapor, turbulence, and atmospheric particulates are created as they relate to line-by-line extinction coefficients for any wavelength. Unlike other models which rely heavily on “standard” atmospheric profiles, LEEDR uses National Oceanic and Atmospheric Administration (NOAA) Operational Model Archive Distribution System (NOMADS) data feeds to provide correlated local weather forecasts for use in profile generation [11]. Our model used a NOMADS data product called Global Forecast System (GFS) which provides LEEDR global weather predictions with 0.5° resolution in 3-hr increments. This coupling allows LEEDR to generate realistic profiles that match real-world conditions for higher-fidelity comparisons to measured data.

LEEDR uses multiple scattering to generate a sky radiance model for a slant path from Dayton, OH to the “uppermost” visible GEO-belt slot for August 26th, 2017. The model was generated for August 26th in 2 hour increments from sunrise to sunset to capture the increasing and decreasing spectral sky radiance as a function of Sun vector alignment with the imaging vector.

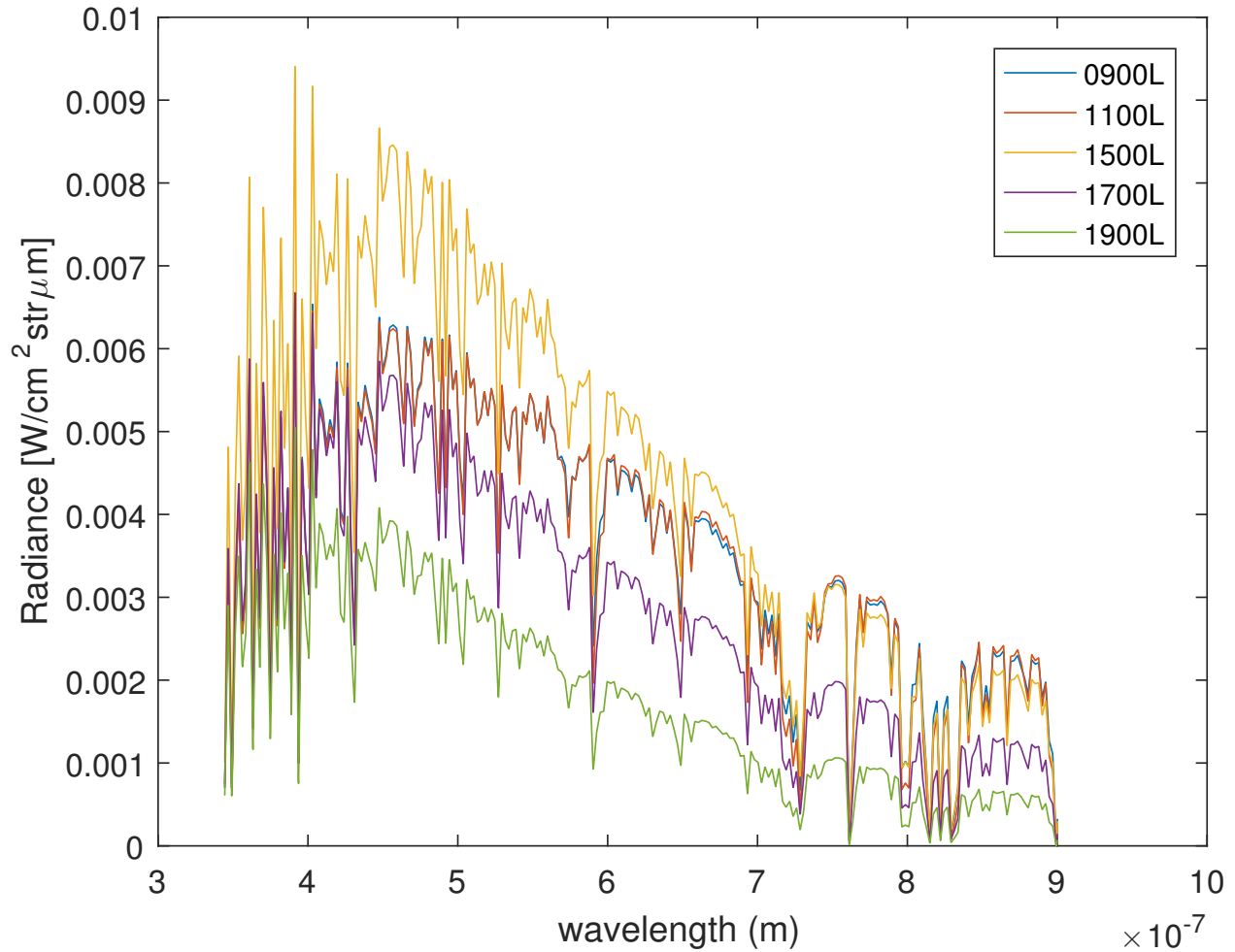


Figure 8: Modeled spectral radiance from LEEDR of the GEO-belt taken over the course of the day on Aug 26th from Dayton, OH.

## 2.2 Results

### 2.2.1 Spectrometer Measurements

Spectral sky radiance measurements were conducted throughout the day on August 26th with exceptionally clear skies. Transient clouds tend to increase the brightness of the detected sky radiance measurement and were avoided for this baseline measurement. The integration time for these measurements was 100ms and each spectra depicted is an average of 10 scans to reduce noise. As expected, the total integrated sky radiance increases as the Sun vectors and imaging vectors align, especially in the visible part of the spectrum (400 to 700nm). In the near infrared (800 to 900nm) the integrated radiance falls as the Sun begins to set, but does not decrease to sunrise levels. This is due to the thermal lag associated with the localized heating of the atmosphere and has further implications for imaging at sunset as compared to sunrise in this region of the spectrum.

### 2.2.2 Measured to Modeled comparison

Figure 9 plots measured data (blue) vs LEEDR generated model data (red) in for a 0900L. The correlation is immediately apparent. The spectra exhibit similar features, with a small offset in the overlay. Perhaps the most significant cause of this error is in the difference in modeled and measured days. Additionally, a micro-focuser element remained in the optical path for the spectrometer measurement and was assumed to

have a negligible effect on the optical throughput and was not modeled. This micro-focuser element will be removed for future measurements to reduce potential sources of error. Both spectra do peak in the visible near 550nm and follow the fundamental Planckian shape. Additionally, the atmospheric attenuation lines were predicted to be more drastic in the model than what was measured. To determine the alignment of spectral features, a subset of H<sub>2</sub>O and O<sub>2</sub> absorption lines were used to compare the spectra[12]. The percent offset of the spectral feature locations from modeled to measured demonstrate the quality of the LEEDR model in predicting molecular resonances and constituent quantities. The results of that analysis are in Tables 1 and 2. Data beyond 900nm is omitted as the linear response of the spectrometer beyond 900nm changes dramatically and makes absolute calibration difficult to achieve.

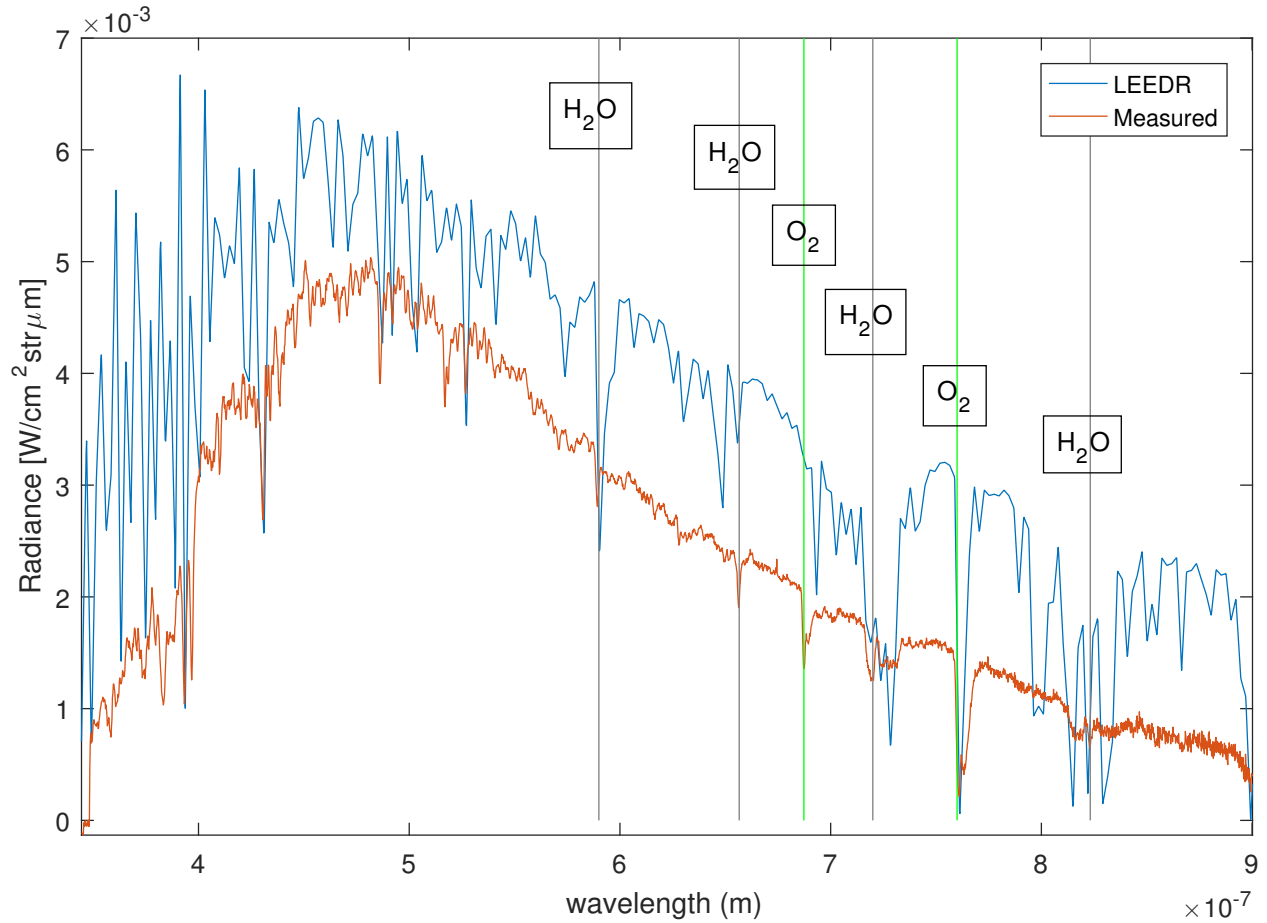


Figure 9: Modeled and measured spectral radiance for 0900L, Aug 26th. Data corrected for optical losses due to telescope mirror coatings, corrector plate and fiber optic cable reflectance. The grey vertical lines represent significant water absorption bands and the green vertical lines represent oxygen absorption bands. For a numerical comparison of these values see Table 1.

Table 1: 0900L Aug 26th Absorption Peak Locations and Total Spectral Radiance Comparisons

Band	Estimate [nm]	Measured [nm]	LEEDR [nm]	$\Delta\lambda$ [nm]	% error
H <sub>2</sub> O 5 $\nu$	590	589.4	590.2	0.8	0.14
H <sub>2</sub> O 4 $\nu$ + $\delta$	650	656.6	655.8	0.8	0.12
O <sub>2</sub> B	690	687.3	693.3	6	0.87
H <sub>2</sub> O 4 $\nu$	720	720.3	728.3	8	1.10
O <sub>2</sub> A	760	761.3	761.3	0	0.00
H <sub>2</sub> O 3 $\nu$ + $\delta$	820	823.2	822.1	1.1	0.13

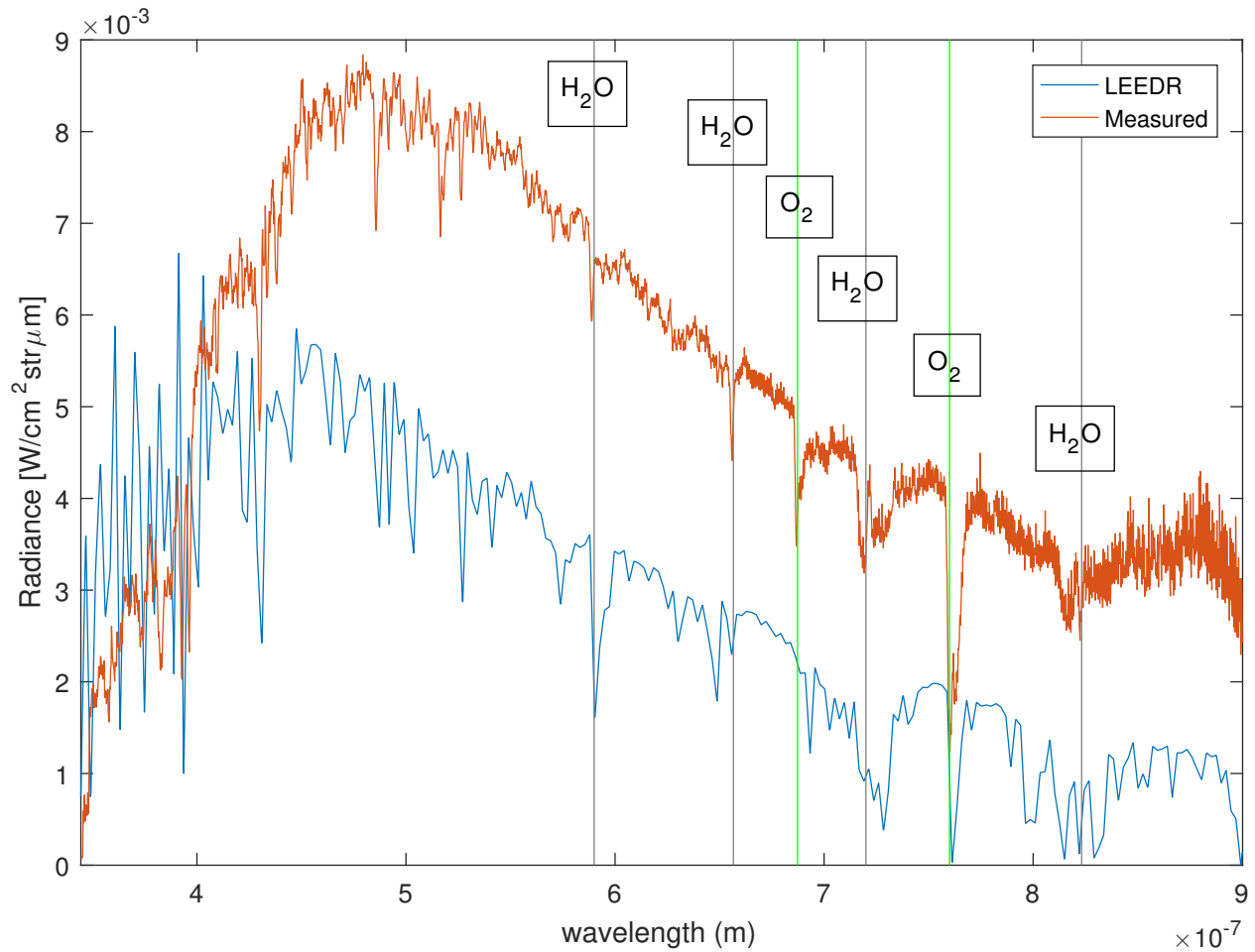


Figure 10: Modeled and measured spectral radiance for 1700L, Aug 26th. Data corrected for optical losses due to telescope mirror coatings, corrector plate and fiber optic cable reflectance. The grey vertical lines represent significant water absorption bands and the green vertical lines represent oxygen absorption bands. For a numerical comparison of these values see Table 2

Table 2: 1700L Aug 26th Absorption Peak Locations and Total Spectral Radiance Comparisons

Band	Estimate [nm]	Measured [nm]	LEEDR [nm]	$\Delta\lambda$ [nm]	% error
H <sub>2</sub> O 5 $\nu$	590	589.4	590.2	0.8	0.14
H <sub>2</sub> O 4 $\nu$ + $\delta$	650	656.6	648.9	7.7	1.17
O <sub>2</sub> B	690	687.3	693.3	6	0.87
H <sub>2</sub> O 4 $\nu$	720	720.3	728.3	8	1.10
O <sub>2</sub> A	760	761.3	761.1	0.2	0.03
H <sub>2</sub> O 3 $\nu$ + $\delta$	820	823.2	822.1	1.1	0.13

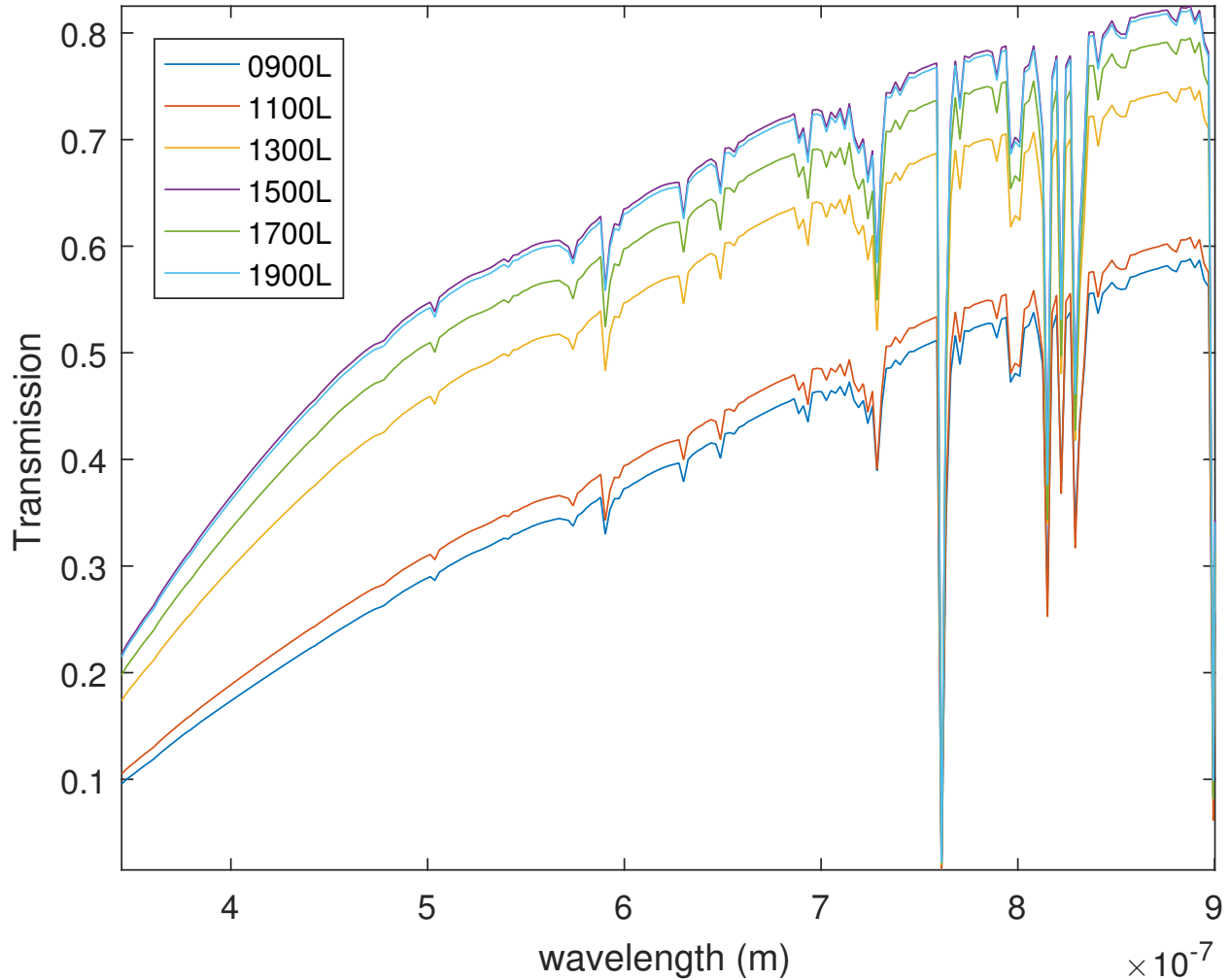


Figure 11: Cumulative Transmission from LEEDR for Aug 26th.

Table 3: Aug 26th Total Spectral Radiance Comparison (from 0.3 to 0.9 $\mu\text{m}$ ) see Figures 9 and 10

	$L_{\text{Measured}} [\text{W}/\text{cm}^2\text{str}\mu\text{m}]$	$L_{\text{LEEDR}} [\text{W}/\text{cm}^2\text{str}\mu\text{m}]$	$\Delta L [\text{W}/\text{cm}^2\text{str}\mu\text{m}]$	% error
0900L	6.638	9.856	3.219	32.66
1700L	14.42	7.618	6.804	47.18

### 3 CONCLUSION AND FUTURE WORK

Preliminary results show that LEEDR path radiance predictions correlate to real-world imaging conditions throughout the day on Aug 26th from Dayton. The results are correlated both radiometrically in terms of intensity and spectrally in terms of peak locations. Preliminary results show that measured spectral radiance correlates to the LEEDR model predictions of spectral sky-radiance for the diurnal noise floor. Vis-NIR radiometric intensity is 30-50% of measured radiance (from Table 3) while spectral feature locations are within 0-1.17% of measured values (from Tables 1, 2).

The close agreement of spectral radiant intensity at each wavelength as well as the total integrated radiance across all wavelengths demonstrates the efficacy of the absolute radiometric calibration method and validates the LEEDR atmospheric model using Global Forecast System (GFS) weather inputs. On this particular date, LEEDR predicted a slightly brighter integrated sky radiance than what was measured at

0900L as in Table 3 and a reduced integrated radiance at 1700L as compared to the measurement also in Table 3. In general, the LEEDR prediction had closer agreement with the measurements at sunrise due to the calmer, less turbulent sky early in the morning.

For spectral comparison between LEEDR and the measurements, we choose to consider H<sub>2</sub>O and O<sub>2</sub> absorption lines in the NIR. The results of the absorption line comparison gives insight into how well LEEDR is able to model the spectral absorption due to the atmospheric constituents. In Table 1 taken from the data at 0900L in Figure 9 there is between 0 and 1.1 nm of difference in the peak locations from the LEEDR model to the measured data. In Table 2 taken from the data at 1700L in Figure 10 there is between 0.2 and 7.7 nm of difference in the peak locations. The close alignment of these peaks in both cases indicates that LEEDR is modeling the fundamental scattering mechanisms quite closely while predicting resonances that result in transmission losses at or near the constituent absorption windows. The higher disparity in spectral alignment between the peaks for the 1700L model is once again due to the increased difficulties in modeling a more dynamic and thus turbulent atmosphere due to the warming atmosphere.

For future models, it will be advantageous to conduct on-site weather measurements or use a particle counter to measure particulates as a function of altitude from the sensor location. As an example, the current models used a constant 69% relative humidity throughout the day to estimate the aerosols at the boundary layer. While this number represents a credible estimate of the average relative humidity on that particular date, the actual relative humidity varied from 39% to 75% on Aug 26th. By measuring this quantity in-situ, we will be better able to model the aerosol-related scattering effects more closely.

Validated models of the sky spectral radiance are critical for the development of daylight custody sensors. Future research will focus on generating measurements at differing locations across the GEO-belt to validate the model under differing atmospheric conditions. In addition, seasonal measurements will compare the Sun's relative proximity to the GEO-belt and give more insight on its effect on spectral sky brightness. It may also be possible to utilize a spectrometer with an InGaAs detector for detection into the short-wave infrared wavelengths (up to 2.4  $\mu\text{m}$ ). In addition, absolute irradiance calibration techniques will be further refined with higher caliber calibration objects to better measure spectral radiance at the sensor and further characterize the optical telescope degradation effects on the detected radiometric signal and predicted utility for daytime SSA collections.

## ACKNOWLEDGMENTS

The authors would like to acknowledge Dr. Earl Spillar and Maj Charlie Bellows at the Air Force Research Laboratory Directed Energy directorate for their guidance in this research. Additionally, Dr. Steve Fiorino, Dr. Kevin Keefer, Jacyn Schmidt and Aaron Archibald of AFIT were all instrumental in generating LEEDR models and the sensor calibration.

## REFERENCES

- [1] Jim, K. T. C., Gibson, B. N., and Pier, E. A., "Daytime Sky Brightness Modeling of Haleakala along the GEO Belt," *Advanced Maui Optical and Space Surveillance Technologies Conference*, Wailea, Maui, Hawaii, 2012.
- [2] Ashley, M. C. B., Burton, M. G., Storey, J. W. V., Lloyd, J. P., Bally, J., Briggs, J. W., Harper, D. A., and Al, A. E. T., "South Pole Observations of the Near-Infrared Sky Brightness," *Publications of the Astronomical Society of the Pacific*, Vol. 108, 1996, pp. 721–723.
- [3] Fiorino, S., Keefer, K., Rice, C., Burley, J., and Schmidt, J., "Characterizing multispectral vertical profiles of aerosol extinction with surface-based measurements," *Imaging and Applied Optics*, Vol. 2017, 2017, pp. 2016–2018.
- [4] Fiorino, S. T., Bartell, R. J., Krizo, M. J., Caylor, G. L., Moore, K. P., Harris, T. R., and Cusumano, S. J., "A first principles atmospheric propagation & characterization tool: the laser environmental effects definition and reference (LEEDR)," *Proceedings of SPIE*, Vol. 6878, SPIE Press, 2008, pp. 1–68780.

- [5] Zibordi, G. and Voss, K., “Geometrical and Spectral Distribution of Sky Radiance: Comparison between Simulations and Field Measurements,” *Remote Sensing and Environment Journal*, Vol. 27, 1989, pp. 343–358.
- [6] Bell, E. E., Eisner, L., Young, J., and Oetjen, R. A., “Spectral-Radiance of Sky and Terrain at Wavelengths between 1 and 20 Microns. II. Sky Measurements,” *Optical Society of America*, Vol. 50, No. 12, 1960, pp. 1313–1320.
- [7] Eismann, M. T., *Hyperspectral Remote Sensing*, SPIE Press, Bellingham, WA, 1st ed., 2012.
- [8] Schwab, M., Averyt, J., Bergkotter, M., and Leyva, A., “Full Spectrum Imaging System,” Tech. rep., The University of Arizona, 2009.
- [9] OceanOptics, “USB4000 Data Sheet,” <https://oceanoptics.com/product/usb4000-uv-vis/>, 2017.
- [10] Toshiba, “CCD Linear Image Sensor TTCD1304AP,” <https://toshiba.semicon-storage.com/ap-en/product/sensor/linear-sensor/detail.TCD1205DG.html>, 2001.
- [11] Fiorino, S. T., Randall, R. M., Via, M. F., and Burley, J. L., “Validation of a UV-to-RF high-spectral-resolution atmospheric boundary layer characterization tool,” *Journal of Applied Meteorology and Climatology*, 2014.
- [12] Hill, C. and Jones, R. L., “Absorption of solar radiation by water vapor in clear and cloudy skies: Implications for anomalous absorption,” *Journal of Geophysical Research*, Vol. 105, 2000, pp. 9421–9428.